The final published version is available at https://doi.org/10.1016/j.cmpb.2026.109246

# *In silico* modelling of aortic annuloplasty: hemodynamic assessment through *in vitro* experiments and *in vivo* MRI

Marta Zattoni[1, 2, 3], Luca Bontempi[4], Steffen Ringgaard[5, 6], Giulia Luraghi[2], Leila Louise Benhassen[5, 7], Peter Johansen[5,8,±], Monika Colombo[1*,±]

[1] Department of Mechanical and Production Engineering, Aarhus University, Aarhus, Denmark
[2] Laboratory of Biological Structure Mechanics (LaBS), Department of Chemistry, Materials and Chemical Engineering "Giulio Natta", Politecnico di Milano, Milan, Italy
[3] Institute of Biomedical Engineering and Technology, Ghent University, Ghent, Belgium
[4] Department of Biomedical Engineering, Thoraxcenter, Erasmus MC, Rotterdam, The Netherlands
[5] Department of Clinical Medicine, Aarhus University, Denmark
[6] Department of MR Research Centre, Aarhus University Hospital, Denmark
[7] Department of Cardiothoracic and Vascular Surgery, Aarhus University Hospital, Denmark
[8] Cardiovascular Experimental Laboratory (CAVELab), Department of Electrical and Computer Engineering, Aarhus University, Denmark
[±] These authors have contributed equally.

**Address for correspondence:**
Monika Colombo, PhD
Cardiovascular Engineering and Biofluids Applications group
Department of Mechanical and Production Engineering
Aarhus University
Katrinebjergvej 89 G, 5132-512
E-mail: mc@mpe.au.dk
ORCID: https://orcid.org/0000-0002-6658-4438

The final published version is available at https://doi.org/10.1016/j.cmpb.2026.109246


# Abstract

Aortic annuloplasty (AA) is an innovative surgical technique for aortic root (AR) enlargement. It is performed by implanting sutures, bands, or rings, either externally or internally the AR, hereby reducing its diameter. This study evaluates the impact of AA approaches on AR hemodynamic by employing a porcine-specific workflow combining *in vivo* magnetic resonance imaging (MRI), *in vitro* experiments and *in silico* fluid-structure interaction (FSI) simulations investigating external single ring AA. CAD models of native and post-annuloplasty ARs were segmented from *in vivo* porcine MRI data and served as the basis for fabricating 3D-printed resin phantoms and implementing computational digital twins. The former were tested on a pulsatile flow-loop, whereas the latter were integrated in FSI simulations, with time-dependent boundary conditions based on the resultant experimental pressure waveforms. Additionally, a proof-of-concept validation of the *in silico* model against *in vivo* data is proposed. Computational results of the two cases were compared in terms of fluid velocity, vorticity, helicity, and wall shear stresses, providing a step towards understanding the complex interactions between the AR and blood flow dynamics. Results suggested that the presence of the ring increased the systolic jet flow and post-valve velocities (three-fold increase), reduced the backward, vortical flow during diastole (~ 9% decrease), and induced modifications in bulk flow and wall shear stresses distribution. Furthermore, the development of an animal-specific digital twin of a post-AA AR represents a significant advancement in the field, providing a valuable tool for future research and for clinical applications to aid AA decision-making process.


**Keywords:** aortic valve, digital twin, fluid-structure interaction simulations, mock circulatory loop, magnetic resonance imaging.

**Abbreviations:**

| | |
|---|---|
| AA | aortic annuloplasty |

| | |
|---|---|
| AR | aortic root |
| CAD | computer-aided design |
| EOA | effective orifice area |
| FSI | fluid-structure interaction |
| LNH | local normalized helicity |
| MCL | mock circulatory loop |
| MRI | magnetic resonance imaging |
| RMS | root mean square |
| WSS | wall shear stress |

# 1. Introduction

Valvular heart disease is a leading cause of cardiovascular morbidity and mortality worldwide.[1] Among aortic valve pathologies, aortic valve regurgitation is related to insufficient leaflets coaptation that may be due to aortic root (AR) lesions, resulting in a retrograde blood flow into the left ventricle. To preserve a physiological ejection fraction, the primary adaptive mechanism of the heart is an increase in left ventricular end-diastolic volume. However, this corrective response leads to a volume overload of the left ventricle that can be incompatible with cardiovascular function[1]. Surgery is the only effective way of intervention and valve replacement has historically been the pillar of treatments[2]. In the last two decades, AR repair, instead, has emerged as a preferable practice for aortic valve regurgitation cases, with a two-fold objective: restore AR lesions while preserving AR leaflets[3]. In this framework, aortic annuloplasty (AA) is an innovative technique defined as the plastic repair of a regurgitant AR by downsizing its annulus, thus limiting annular expansion, one of the main risk factors for aortic valve regurgitation recurrence[4]. Several AA concepts have been proposed using sutures, bands, rings, either externally or internally of the AR, and clinical results are encouraging[5]. However, this technique is still not widely used due to a lack of standardization, as there is no gold standard for AA, neither in terms of shape, position, nor material[6]. More investigation is needed to determine which method is more effective.

Notably, biomechanical studies examining AA are very limited in number. De Kerchove *et al.* used an in-house pulsatile left heart simulator to evaluate a novel AA device for the treatment of aortic annular dilation, establishing a promising starting point for further experimental evaluation of the hemodynamic of AA approaches[7]. Similarly, Benhassen *et al.* conducted an *in vitro* study on a customized left heart simulator to characterize the functional and dynamic properties of single- and double-ring AA[8]. Despite experimental studies being the first step of valve repair systems validation process according to ISO guidelines, with the significant advancements

in imaging techniques and improvements in computational architecture, numerical models have emerged as a powerful tool in cardiovascular research. Recent U. S. Food and Drug Administration approval recognized *in silico* simulations as an alternative method for medical devices testing[9]. Specifically, fluid-structure interaction (FSI) simulations coupling finite element modelling and computational fluid dynamics have the potential to shed light on phenomena that cannot be captured *in vitro*. However, lack of validation is keeping from integrating these methods in clinical care[10] and for this reason cardiovascular research is focusing on complementing *in vitro*, *in vivo*, and *in silico* data, that can provide robust and validated results. In our previous work, we showed how a systematic integration of mock circulatory loop (MCL) experiments and non-invasive 4D flow magnetic resonance imaging (MRI) can complement an idealized AA computational model and contribute to the validation of an high-fidelity FSI simulation, also establishing the only example of AA digital twin available in literature up to date[11].

The present study aims at advancing AA hemodynamic knowledge by developing the first porcine-specific AR digital twin through a comprehensive workflow of *in vivo* MRI, *in vitro* flow experiments and *in silico* FSI simulations, investigating external single ring AA procedure[6].

## 2. Materials & Methods

The initial phase of the study involved the analysis and elaboration of two *in vivo* porcine MRI scans: one native and one post-AA. Porcine-specific computer-aided design (CAD) models of the AR were constructed and were subsequently first employed in an experimental investigation, as well as in a computational analysis, afterwards. In the former, 3D-printed phantoms of the AR were fabricated and integrated in a MCL, where pressure and flow data harvesting was conducted. In the latter, two porcine-specific digital twins of the AR were developed and modelled through FSI approach, utilizing the previously collected experimental data to define the governing boundary conditions. Lastly, *in silico* findings were compared against *in vivo* MRI data to assess the reliability of the methodology and the results (Figure 1).

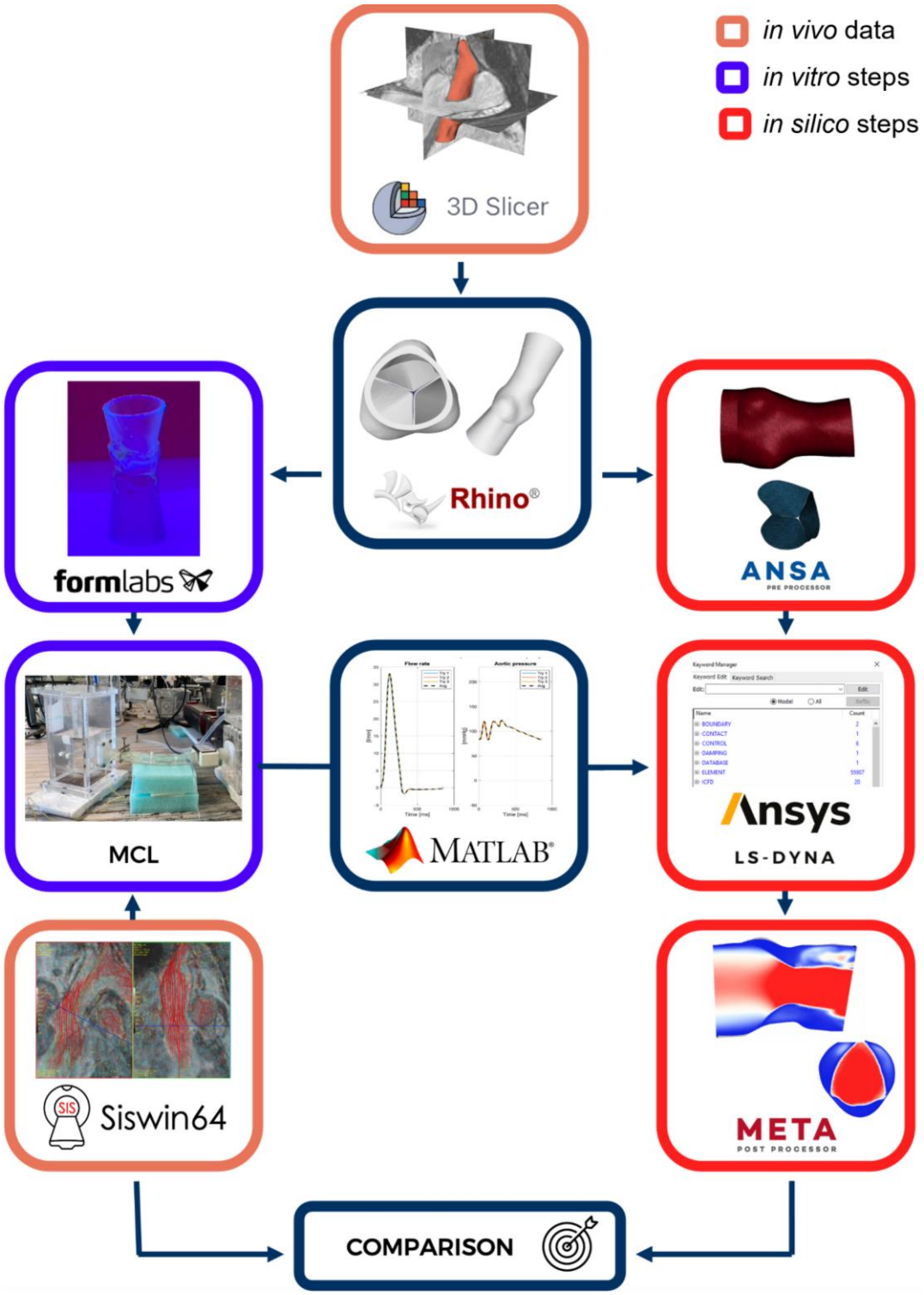


**Figure 1: Workflow of the study and software**. Segmentation and post-processing of *in vivo* MRI data to produce porcine-specific CAD models of the AR used in flow-loop experiments and FSI simulations. Comparison of computational results with *in vivo* porcine data to assess the fidelity of AA digital twin.

## 2.1 *In vivo* data processing

*In vivo* MRI data of one native and one post-AA 80 kg pigs from a previous study were considered[12]. MRI acquisitions were performed with a 1.5 T magnetic resonance scanner (Achieva dStream, Philips Medical Systems, Best, The Netherlands) to collect a 3D stack of images acquired with a balanced steady-state free-precession sequence covering the heart in the diastolic phase with a 1.3 mm slice thickness, reconstruction matrix 480 x 480, repetition time 4.40 ms, echo time 2.20 ms, flip angle 90°, in-plane resolution 1.25 x 1.25 mm; as well as 4D flow sequences in 20 phases/cardiac cycle in the antero-posterior, right-left, and foot-head directions, with 2.5 x 2.5 x 2.5 $mm^3$ voxel size, 8° flip angle, 2.10 ms echo time, 3.87 ms repetition time. Velocity encoding was set at 170 cm/s with the aim of successfully investigating high AR systolic flow rates. Cardio-respiratory gaiting was also integrated throughout the duration of the scan.

Results were visualized and post-processed using Siswin64, an in-house MRI analysis software (see *Supplementary Figure S1*). Firstly, images covering the heart were used to perform a semi-automated segmentation of the AR diastolic configuration with 3DSlicer (v5.6.2, www.slicer.org). Secondly, the segmented models were further elaborated in Rhinoceros (v8, Robert McNeel & Associates, Seattle, WA, USA). As manual segmentation of the aortic leaflets proved to be unfeasible due to MRI insufficient contrast and resolution, they were manually constructed according to simplifying assumptions and by identifying several reference points[13]. More specifically, from the *in vivo* axial view of the AR, commissures and shape of the leaflets' margins were identified, and reproduced in the axial plane of the AR in Rhinoceros, while the three leaflets' attachments on the wall of the sinuses were created following the shape of the sinuses of Valsalva.

## 2.2 Mock circulatory loop experimental investigation

Starting from CAD models, the experimental investigation was conducted consistently with our previous work on idealized AA[11], and involved the fabrication of porcine-specific 3D-printed resin

phantoms of native and post-AA ARs as well as their testing on a pulsatile *in vitro* MCL (Figure 2). Some additional modifications to the models were incorporated before stereolithography printing. Namely, the thickness of the wall and leaflets of the AR was set at 1.5 and 0.4 mm, respectively. The former ensured a compliance value of 1 ml/mmHg to provide AR distensibility, aligning with AR physiological values[14,15], whereas the latter represented the minimum value that enabled successful 3D-printing[11]. Additionally, connection parts tailored to mounting the phantoms in the MCL were designed. The final geometry was then divided into three portions and each part was printed separately to facilitate the supports removal, which proved to be challenging especially around the leaflets. All models underwent 3D-printing through the same methodology. They were then transferred to PreForm (v3.34.2, Formlabs, Somerville, MA, USA) to adjust orientation on the printing plate and to define support material placing.

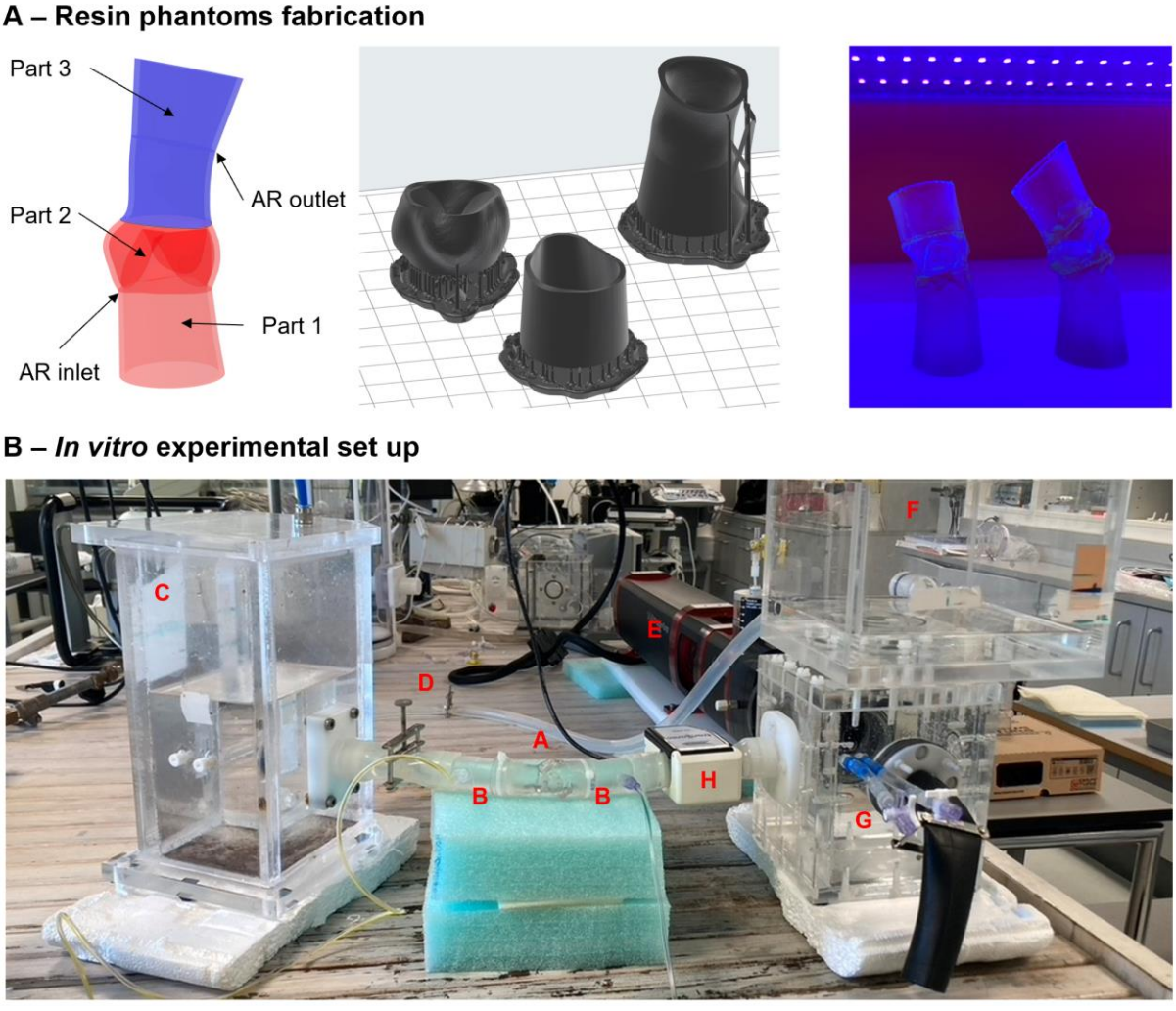

**Figure 2: *In vitro* investigation.** A) Resin phantoms fabrication steps from CAD model design, to support placing, 3D printing and UV curing. B) CAVELab MCL set up consisting of AR phantom (A), fluid-filled pressure sensors (B), compliance chamber (C), peripheral resistance clamp (D), electromechanical piston pump (E), atrial chamber (F), ventricular chamber (G) and flowmeter (H).

The choice of the printing material fell on Elastic 50A V1 resin, which was used in Form 3B+ printer (Formlabs, Somerville, MA, USA, 0.25 mm resolution on the x-y plane, 0.3 mm layer thickness). After printing, the pieces were cured under UV light at 60° C for 20 minutes, then, all the supports were removed, and the three portions of each AR model were glued together using the same resin. Finally, the ARs underwent a second 20-minute curing session after which they were rinsed in isopropyl alcohol. Thereafter, samples were mechanically characterised according to ISO 37-1:2017 guidelines for the determination of tensile stress-strain properties of rubber, vulcanized or thermoplastic materials, as explained in our previous work[11,16]. The resin exhibited an elastic modulus of approximately 1.8 MPa for small strains below 25% (*Supplementary Figure S2*).

The MCL was set to reproduce *in vitro* the left heart pulsatile behaviour using demineralized water as test fluid and was equipped with a transient time flowmeter (ME-20PXL, Transonic Systems Inc., Ithaca, NY, USA) and fluid-filled pressure catheters for flow and pressure monitoring upstream and downstream the AR. Simultaneous acquisition of data at a sampling rate of 1000 Hz was accomplished using a multipurpose 16-bit data acquisition module (NI USB-6259, National Instruments, Austin, TX, USA). Experiments complying with ISO 5910:2018 human adult normotensive conditions were conducted for both native and post-AA models to replicate the physiological functioning of the AR within the MCL and investigate the influence of AA on its hemodynamic. MCL resistance and compliance were adjusted to achieve the following target values: an heart rate of 70 bpm, a cardiac output of 5 l/min, a maximum aortic pressure of 120 mmHg, a minimum aortic pressure of 80 mmHg, a maximum ventricular pressure of 120 mmHg, and minimum ventricular pressure around 0 mmHg[17]. To ensure statistical reliability and repeatability each acquisition involved the recording of 15 cardiac cycles over three different acquisitions, in between which the pump was shut off and restarted. Data post-processing was performed in MATLAB

(vR2024b, MathWorks, Natick, MA, USA). For each AR model, mean raw waveforms of aortic pressure, ventricular pressure, and flow rate were computed. Noise filtering was implemented with a third order lowpass Butterworth filter with a cutoff frequency of 15 Hz. Figure 3-B shows the final pressure tracings resulting from the MCL measurements and imposed as boundary conditions of the later computational analyses, in the case of native model (*Supplementary Figure S3* shows the raw data before filtering). Additionally, hemodynamic parameters were investigated according to ISO guidelines on *in vitro* cardiac valve repair devices testing (Annex M)[17]. Indeed, results are presented in terms of the following parameters: (a) cycle rate, defined as the number of complete cycles per unit of time and expressed in cycles/min; (b) systolic duration as a percentage of the cycle time, defined as the portion of cardiac cycle time corresponding to ventricular contraction and equal to the duration of forward flow; (c) transmural pressure, defined as the time-averaged arithmetic mean value of the pressure difference across a heart valve during the positive differential pressure period of the cycle in mmHg; (d) mean arterial pressure over the whole cycle, defined as the time-averaged arithmetic mean value of the arterial pressure during one cycle in mmHg; (e) mean and root mean square (RMS) flow rates through the AR in l/min; (f) forward flow volume, defined as the volume of flow ejected through the heart valve in the forward direction during one cycle, not including any regurgitant flow through the valve in ml; (g) regurgitant volume, defined as the volume of fluid that flows through a heart valve in the reverse direction during one cycle in ml; (h) effective orifice area (EOA), namely the measurements of the valve's flow-passing capacity, derived from flow and pressure data and expressed according to Equation (1), where $q_{v\ RMS}$ is the RMS of the forward flow in ml/s during the positive differential pressure period, $\Delta p$ is the mean pressure difference in mmHg measured during the positive differential pressure period, and $\rho$ is the density of the test fluid in g/cm$^3$.

$$EOA = \frac{q_{v\ RMS}}{51.6 \cdot \sqrt{\frac{\Delta p}{\rho}}} \quad (1)$$

## 2.3 Fluid-structure simulation computational analysis

Porcine-specific digital twins of the native and post-AA models were developed through FSI modelling in LS-DYNA (R14.1, Ansys, Canonsburg, PA, USA). Meshing was performed in ANSA (v24.1.1, BETA CAE Systems, Switzerland), where the aortic leaflets and walls, inlet and outlet of the AR were discretized in triangular shell elements (Figure 3-A) and modelled using reduced integrated shells with 3 thickness integration points. This decision was driven by the need to minimize computational costs and it was supported by literature, as it has been shown that modelling heart valve leaflets with shell-type elements is the best compromise between the computational efficiency and the model complexity[18]. The fluid volume was autogenerated in LS-DYNA from the fully enclosed shell meshes. Accordingly, to the results of a structural sensitivity analysis, element length was set at 0.4 mm, as for any further refinement computational time increased from less than 1 h to more than 6 h, while relative error of all variables of interest improved less than 4% (*see Supplementary Figure S4-5*). A uniform discretization of the aortic wall was generated with 44,746 and 32,562 elements, and of the aortic valve with 11,161 and 7,365 elements, for the native and post-AA models, respectively. The fluid domain consisted of 1,722,807 elements in the native model and 1,082,602 elements in the post-AA model.

The final published version is available at https://doi.org/10.1016/j.cmpb.2026.109246

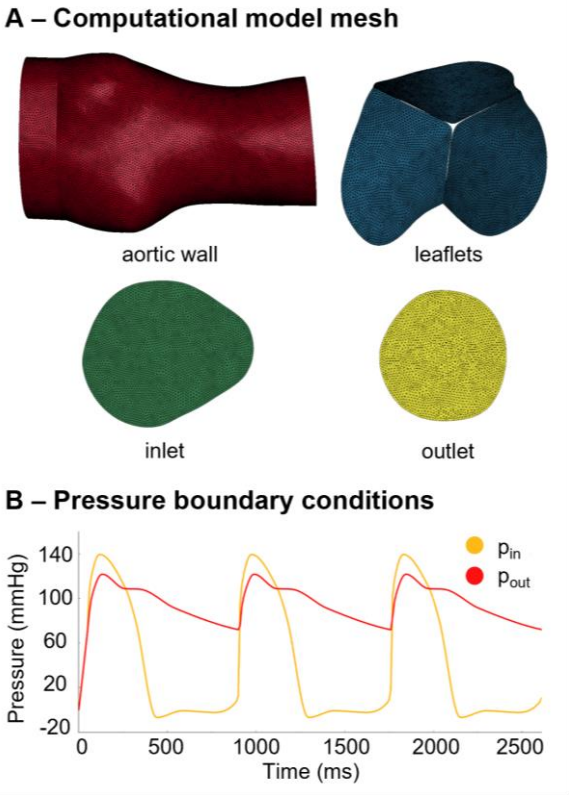


**Figure 3: *In silico* model.** A) Different components of the native computational model meshed with triangular shells. B) Pressure boundary conditions imposed at the inlet (ventricular pressure, $p_{in}$) and outlet (aortic pressure, $p_{out}$) of the native model in the FSI simulations.

To match the experimental conditions, the aortic leaflets and aortic wall thicknesses were defined at 0.4 and 1.5 mm, respectively, and assuming that the AR would not experience large strains throughout the cardiac cycle both parts were assigned the linear elastic material properties of Elastic 50A resin: 1,100 kg/m$^3$ density, 1.8 MPa Young's modulus and 0.45 Poisson's coefficient[11]. The elements within the AR volume were modelled with a Newtonian model and mimicked demineralized water properties: 997 kg/m$^3$ density and 0.0012 Pa·s dynamic viscosity.

Since there is no conclusive evidence supporting that the employed 2D and 4D-flow MRI imaging could describe the characteristics of typical turbulent flow, a laminar model was employed, as also previously done in our group. Experimental aortic and ventricular pressure curves were imposed as boundary conditions at the inlet and outlet of the AR, respectively, as shown in Figure 3-B. On the internal AR surface, no-slip condition was applied. Leaflets coaptation was modelled through a penalty contact algorithm (automatic single surface, in LS-DYNA), setting both static

and dynamic friction coefficients to 0.05, viscous damping coefficient to 50, scale factors on the surfaces to 0.5 and scale factor applied to contact thickness to 1.2.

Time discretization was dynamically updated to satisfy the Courant-Friedrichs-Lewy condition, to optimize numerical stability throughout the analysis. The Lagrangian initial time step was set to 0.1 ms, restraining the allowable range between 0.1 and 5.0 ms, and was updated using the central difference method to ensure second-order accuracy. The Newmark scheme was employed for the nonlinear analysis, with time integration constants $\gamma$ and $\beta$ set to 0.60 and 0.38, respectively.

To reach a steady state, three complete cardiac cycles were simulated[11]. The structural, fluid-dynamic and FSI problems were all solved with an implicit method, along with an Arbitrary Lagrangian-Eulerian method for the interface mesh kinematics. This approach consists in a segregated scheme, where the fluid and structure are solved in a strong 2-way coupled manner. Simulations were run on 28 CPUs of an Intel Xeon64 with 250 GB of RAM and took approximately 17.9 hours. Post-processing of results was performed with META (V24.1.1, BETA CAE Systems, Switzerland) and ParaView (v5.11.0, Sandia National Labs, Kitware Inc., Los Alamos National Labs).

## 2.4 Statistical and hemodynamic analysis

The normality of the velocity distributions was assessed using the Kolmogorov-Smirnov test. Based on the results, non-parametric tests were employed, and the values were expressed as the median and interquartile range (IQR). The comparison between groups was conducted using the Kruskal-Wallis test or Mann-Whitney U test where appropriate. All analyses were performed in MATLAB, assuming a significance level of 5%.

Hemodynamic variables reported in the following section were computed along different regions of the models, defined between three cut planes across the AR as shown in Figure 4-A. Namely, the bottom, mid and top planes separate pre-valve, sinuses of Valsalva and post-valve

volumes. For both models, all results were investigated at peak systole (t = 200 ms) and late diastole (t= 860 ms) of the third cycle.

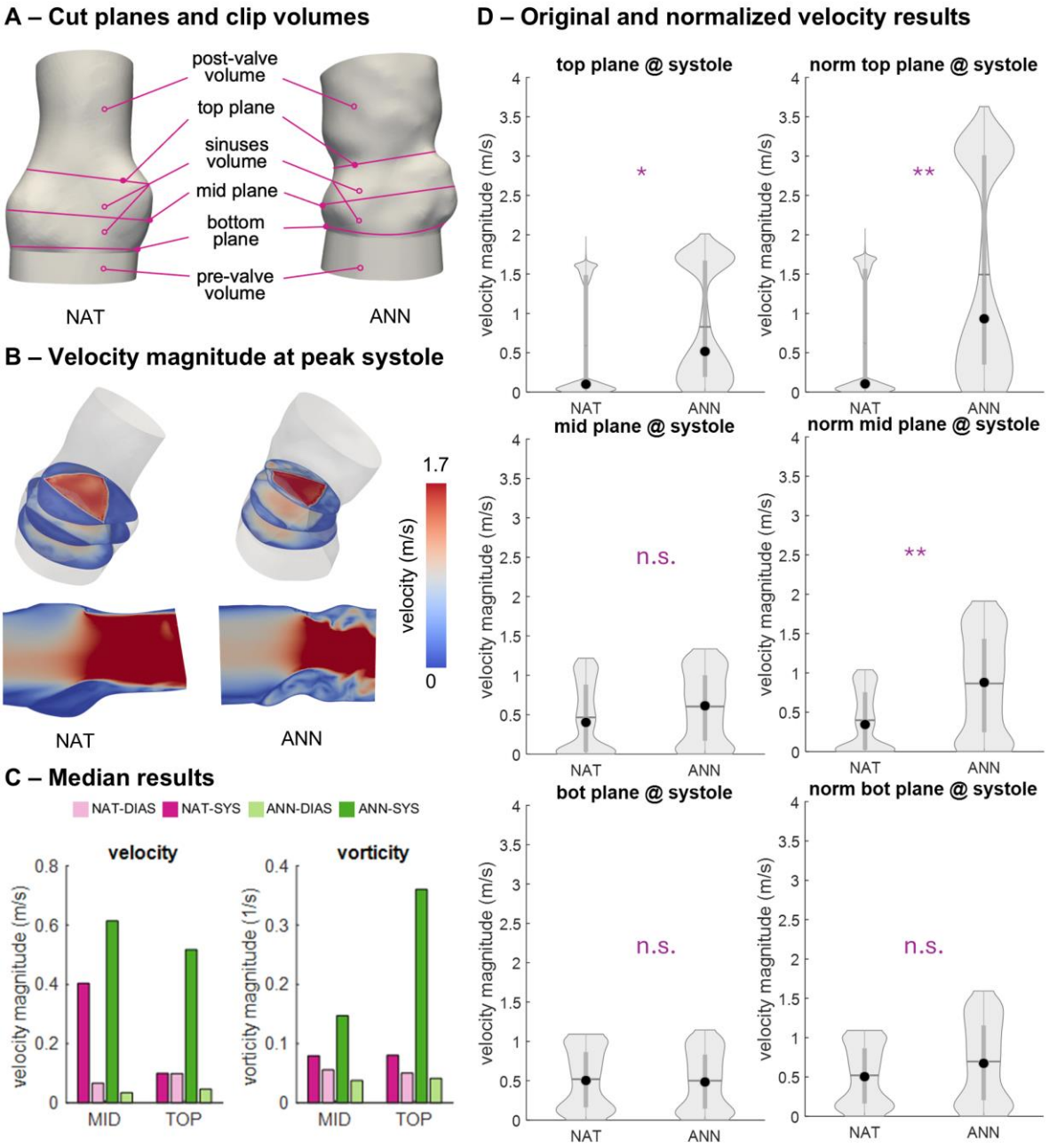


**Figure 4: Hemodynamic results on cut planes**. A) Scheme of cut planes and clip volumes considered during results post-processing and data visualization. B) Velocity magnitude contour plots for native and post-AA models at peak systole. C) Velocity and vorticity magnitude median results on mid and top cut planes at peak systole and late diastole for native and post-AA models. D) Velocity magnitude distribution on top, mid and bottom planes at peak systole in native and post-AA models. Results are compared with normalized results with respect to the bottom plane area. *: *p*-value < 0.05; **: *p*-value < 0.0005; n.s.: not significant.

Both near-wall and bulk flow indices, specifically wall shear stress (WSS)[19,20] and local normalized helicity (LNH)[21,22], were evaluated according along with velocity and pressure field. The former was computed in ParaView by extracting vessel surface, generating normals, and resampling the velocity gradient from the volume (see SI for detailed calculation steps and filters). The viscous traction was obtained as detailed in Equation (2). The tangential component was then isolated by removing the normal projection, and its magnitude was reported as WSS. LNH was instead computed as reported in Equation (3).

$$\boldsymbol{\tau} = \mu((\nabla \boldsymbol{v} + (\nabla \boldsymbol{v})^T) \cdot \boldsymbol{n}) \quad (2)$$

$$LNH = \frac{\boldsymbol{v} \cdot \boldsymbol{\omega}}{|\boldsymbol{v}| \cdot |\boldsymbol{\omega}|} \quad (3)$$

Where $\mu$ is the viscosity, $\boldsymbol{v}$ is the velocity, $\boldsymbol{n}$ is the normal at the aortic wall and $\boldsymbol{\omega}$ is the vorticity.

### 2.5 Proof-of-concept validation: acute AA surgery conditions

An additional series of 'MRI-based' acquisitions was performed on the MCL and results were used to implement corresponding FSI simulations, following the same procedure described previously. Herein, the MCL target values were derived from porcine *in vivo* data, thus reproducing porcine-specific conditions and establishing results that have the potential to be compared with 4D flow MRI with the aim of validating the workflow against *in vivo* evidence.

## 3. Results

### 3.1 Fluid domain: AR hemodynamic

Experimental and computational resultant pressure and flow rate waveforms at the inlet and outlet of the AR were evaluated according to ISO 5910:2018 (Annex M) hemodynamic performance parameters[17]. The comparison for physiological condition cases is showed in Table 1, while *Supplementary Table S1* reports the results of MRI-based experiments and simulations. Some discrepancies are still evident for flow-related parameters, presumably due to issues in capturing the leaflets' mechanics while modelling them. However, this drawback was considered acceptable in the framework of the following investigation.

**Table 1:** Hemodynamic assessment of MCL and FSI analyses results for physiological conditions ( NAT: native; ANN: annuloplasty).

| | **experimental MCL** | | **computational FSI** | |
|---|---|---|---|---|
| | **NAT** | **ANN** | **NAT** | **ANN** |
| **Cycle rate** (cycles/min) | 70 | 70 | 69.8 | 71.4 |
| **Systolic duration** (%) | 33 | 33 | 28 | 29 |
| **Mean arterial pressure** (mmHg) | 95.9 | 101.0 | 95.3 | 99.9 |
| **Mean transvalvular pressure** (mmHg) | 15.6 | 45.5 | 11.2 | 16.6 |
| **Mean flow rate** (lpm) | 5.3 | 5.0 | 1.7 | 1.7 |
| **RMS flow rate** (lpm) | 12.1 | 11.3 | 7.8 | 5.7 |
| **Forward flow volume** (mL) | 81.4 | 76.4 | 54.6 | 36.8 |
| **Regurgitant flow volume** (mL) | 5.7 | 5.2 | 23.5 | 10.6 |
| **EOA** ($cm^2$) | 2.0 | 1.0 | 1.2 | 0.8 |

Velocity magnitude contour plots computed on cut planes along the AR at peak systole and reported in Figure 4-B display some differences in the velocity field for native and post-AA cases, especially in the sinuses of Valsalva and post-valve volumes. Median velocity and vorticity calculated on the same planes exhibit higher values at peak systole and lower values at end diastole in the post-AA case (Figure 4-C): median velocity at systole in the post-AA model is three-fold the native one at the top plane, while it is only 1.5-fold at the mid plane and a similar behavior is encountered in the vorticity as well, which was almost doubled at mid plane and about seven-fold at the top plane. Notably, at the diastole, the median velocity and vorticity at both planes were higher in the native configuration. Figure 4-D reports the normalization of the velocity distributions with respect to a scale factor accounting for the ratio between the bottom area of the two models, which allowed a direct comparison of the velocity fields, as if ARs had same cylindrical shape. These results demonstrated that the presence of the AA ring induces a statistically significant increase in the velocity distributions in the mid and top planes, as compared to the native case. Further information on the normalization process and the statistically significant differences between velocity distributions is provided in SI and Figure S6 and S7.

Figure 5-A shows the median LNH values for native and post-AA models at peak systole and end diastole, computed separately on the pre-valve, sinuses and post-sinuses volumes. A visualization of a threshold contour plots is reported in Figure 5-B, highlighting the elements of the fluid volume of the AR with a LNH above 0.7 at peak systole. In the native case, they are distributed along the entire AR, whereas in the post-AA condition, they are more concentrated in the post-valve volume.

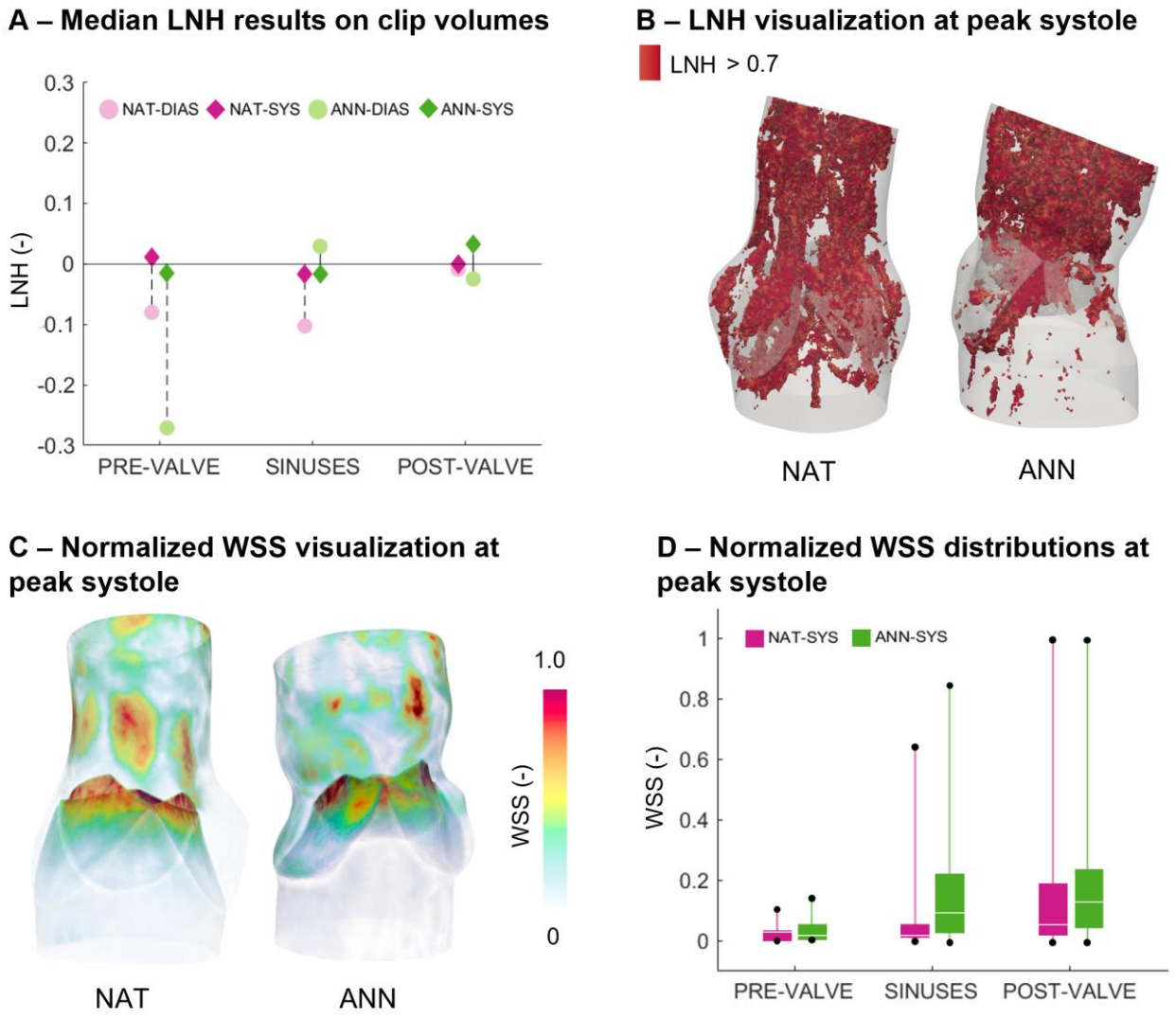


**Figure 5: Hemodynamic results on clip volumes**. A) Median LNH results on clip volumes for native and post-AA models at peak systole and late diastole. B) LNH threshold visualization of values above 0.7 at peak systole for native and post-AA models. C) Normalized WSS contour plots at peak systole for native and post-AA models. D) WSS distributions on clip volumes for native and post-AA models normalized with respect to the maximum WSS value for each case.

Lastly, an investigation of the WSS was performed. In Figure 5-C it is evident how higher WSS are present on the aortic leaflets close to their free margins and closed to the post-valve aortic walls. Normalization of results in this case was obtained using the maximum WSS value to facilitate the comparison of native and post-AA cases (Figure 5-D). The former exhibits higher WSS values consistently throughout the three AR cut planes.

## 3.2 Structural domain: leaflets dynamics

An assessment of the aortic leaflets kinematics and their stress states is reported in Figure 6, which presents a visual comparison of the top view of the leaflets' displacement between the native and post-AA models at peak systole and end diastole together with the contour plots of the Von Mises stresses. Different main phases can be identified when investigating the leaflets motion: an opening phase, that culminates in the most opened valve configuration at peak systole, a closing phase, and a closed phase throughout the duration of diastole.

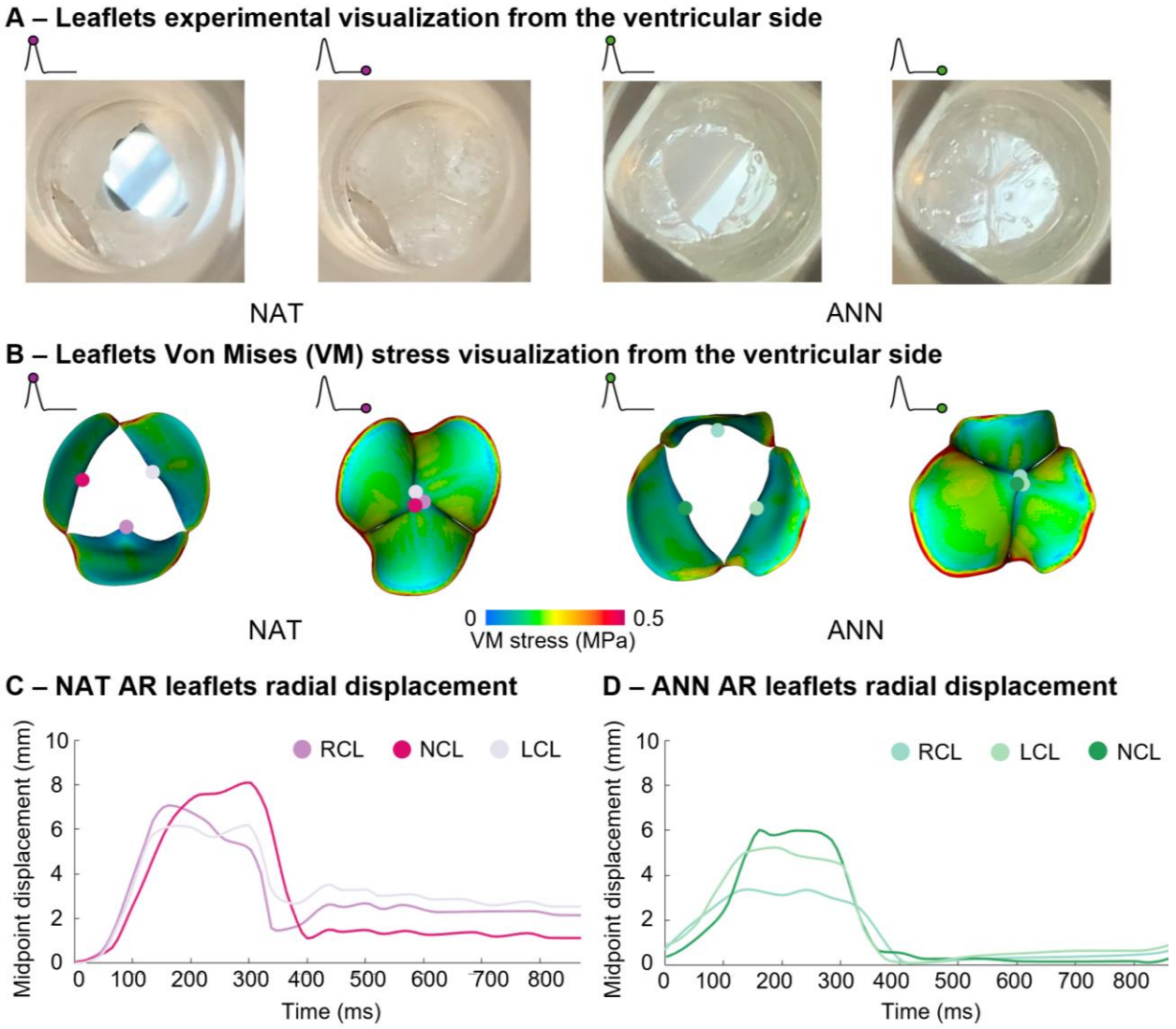


**Figure 6: Structural results on aortic leaflets**. A) Visualization of aortic leaflets opened and closed configuration during experiments for native and post-AA models. B) Visualization of aortic leaflets Von Mises stress for native and post-AA AR models at peak systole and end diastole. C) Midpoint radial displacement results throughout the third cardiac cycle for right coronary (RCL), left coronary (LCL) and non-coronary (NCL) leaflets in native model. D) Midpoint radial displacement results throughout the third cardiac cycle for right coronary (RCL), left coronary (LCL) and non-coronary (NCL) leaflets in post-AA model.

Leaflets' opening dynamics shows some differences between the two models, related to their different geometrical features and boundary conditions. In the native model, at peak flow rate through the aortic annulus, the midpoints of the leaflets' free margins reached a maximum displacement of 8 mm with respect to the initial unloaded configuration, whereas in the post-AA model, the maximum displacement was 6 mm. Notably, maximum displacements are reached during peak systole in both cases. Moreover, the leaflets exhibit similar orifice shapes and stress patterns throughout the cardiac cycle. The Von Mises stresses magnitude is higher during diastole,

when the valve is fully closed, than during peak systole. At peak systole, the region where stresses are mostly located is near the commissures, along the leaflets' attachment to the AR wall, while during diastole, these are located at the leaflets' coaptation area and along their attachment edges. Von Mises stress magnitude on the valve leaflets fell between 0 and 0.4 MPa. These findings are consistent with FSI simulations reported in literature[23–25].

## 3.3 Integration of results: MRI-based assessment

With the aim of performing a consistent comparison between *in vitro* and *in silico* results with *in vivo* porcine MRI, along with the physiological hemodynamic scenarios described above, additional FSI models were run following the same methods described above but imposing MRI-based flow conditions and related *in vivo* pressure measurements as target values of the MCL in the experiments and boundary conditions in the simulations, instead of target physiological conditions. While the comparison of AR hemodynamics between the native and post-AA models was not feasible in this case, due to the different imposed boundary conditions – which would overcomplicate the comparison of the fluid fields – the additional FSI simulations confirmed the applicability of the entire workflow in different scenarios. Above all, MRI-based models allowed a qualitative comparison of the computational results against MRI 2D flow and 4D flow data (*Supplementary Figure S6*). Indeed, it was possible to perform an initial step towards validation of porcine-specific AA digital twin against *in vivo* evidence.

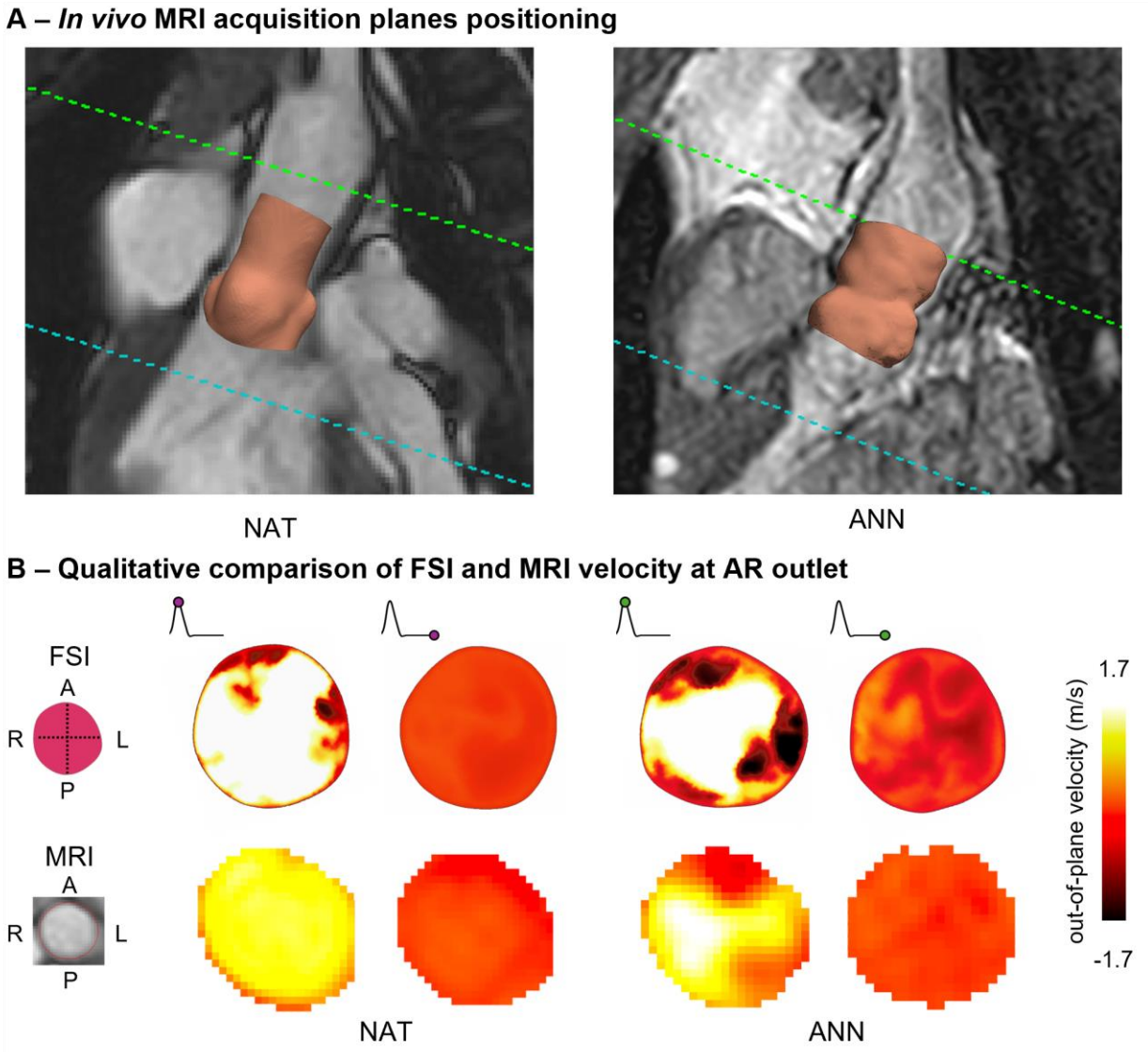


**Figure 7: MRI-based assessment of hemodynamic results**. A) MRI view of the porcine hearts showing the positioning of the two available planes to compute AR flow rate waveform with respect to the segmented models from in vivo MRI data (green: Qoutflow; light blue: Qinflow). B) Out-of-plane velocity component contour plots for FSI simulations and MRI in vivo data at the outlet of the AR for native and post-AA models. Contour plots are reported with the same orientation, which is detailed in the two maps on the left of the figure for both MRI and FSI (A: anterior; P: posterior; R: right; L: left).

Results were assessed in terms of contour plots of the out-of-plane component of the velocity computed from MRI $Q_{outflow}$ planes (Figure 7-A, green dashed lines) and from the aortic outlet plane of the FSI simulations, for both native and post-AA models. Qualitative contour plots at systole and diastole are shown in Figure 7-B. In general, the velocity distributions showed a good qualitative agreement between FSI and MRI, especially in the post-AA model, where the triangle-shaped pattern is clearly visible at peak systole. The main relevant differences are evident in the

native model at peak systole. Herein, as shown at the top of Figure 7, the results were acquired in the ascending aorta, further from AR outlet, and characteristic features of AR outlet hemodynamics are not visible.

# 4. Discussion

This study aimed at developing an integrative framework to enhance the understanding of the impact of the AA surgical procedure on AR hemodynamics. Specifically, the first porcine-specific AR digital twin was developed through a comprehensive workflow that integrates *in vivo* MRI, *in vitro* flow experiments, and *in silico* FSI simulations. The focus was on investigating the external single ring AA procedure, providing valuable insights into its efficacy and potential for clinical application. Based on our previous study and on other recent works[11,26–28], the integration of *in vivo* MRI data with *in vitro* flow experiments and *in silico* FSI simulations provided a robust framework for assessing the hemodynamic performance of AA. This comprehensive methodology addresses the current lack of standardization in AA techniques,[6] offering a potential pathway towards establishing a gold standard for AA procedures.

The simulations conducted under physiological conditions served as a benchmark to confirm the capability of the porcine-specific models in accurately replicating the characteristic features of AR function. Moreover, they highlight the significance of using patient-specific (or animal-specific) geometries and boundary conditions, as the differences in hemodynamics results between native and post-AA showed how those substantially influence simulations outcomes. Furthermore, MRI-based conditions simulations mimicking acute conditions after surgery were implemented to specifically investigate the effects of AA surgery on AR hemodynamics.

The presented findings from this study are consistent with previous experimental studies, such as those conducted by De Kerchove *et al.* and Benhassen *et al.*,[7,8] which highlighted the importance of AA in treating aortic annular dilation and characterizing the functional and dynamic properties of AA devices. Through the complementary techniques used in this study, we were able

to quantify the effect of a single ring AA on the AR flow features and stresses. Starting from the global hemodynamic considerations of the experimental measurements (Table 1), the AA relevantly shifted the mean pressure difference, with a three-fold increase in case of the post-AA model. The post-AA model presented also lower forward (~ -6%) and regurgitant (~ -9%) flow volumes, along with a halved EOA as compared to the native case. While EOA in the computational model is notably lower than the experimental one, the trend of its reduction moving from native to annuloplasty model is found in both the methodologies. This also suggests that further refinement of the computational model is needed to fully meet the experimental conditions.

In terms of local hemodynamics available from the FSI analyses, the normalization based on geometrical factors, along with the identical boundary conditions imposed to the models, allowed a direct comparison of the velocity field, as if ARs had same cylindrical shape[20]. This approach demonstrated that the presence of the AA ring induces a statistically significant increase in the velocity distributions in the mid and top planes, as compared to the native case. The main velocity difference is present during systole along the top plane, close to the STJ, where the median velocity and vorticity were relevantly larger than in the native case. It is also worth noting that in diastole the same median values were lower in all planes for the annuloplasty model. These findings suggest that the presence of the ring increased the systolic jet flow and post-valve velocities, while reducing the backward, vortical flow during diastole. Lastly, helicity measure LNH and WSS results proved that the AA ring induced many modifications in the bulk flow as well as on the wall with significantly larger WSS in the sinuses surface, as compared to the native case. Regarding the structural modifications induced by the AA ring, the Von Mises stress analysis showed consistency with previous findings for both the AR models. However, the assessment of the aortic leaflets' kinematics revealed notable differences in terms of maximum displacement of the leaflets' free margin at peak systole between the native (8 mm) and post-AA models (6 mm). This reduction in displacement, probably induced by the AR different geometry, confirms the capability of our model to effectively represent the AA procedure effect of limiting the annular expansion, which re-

establishes sufficient leaflet coaptation, a feature that is considered crucial for preventing aortic valve regurgitation recurrence. Lastly, we showed a proof-of-concept of AA digital twin validation, which can be performed by leveraging *in silico* results reflecting MRI-based conditions and *in vivo* MRI 2D flow and potentially 4D flow MRI.

Despite the promising results, there are several limitations to this study that should be acknowledged. The use of two different porcine AR models, which, firstly, may not fully capture the complexities of human AR pathology, and secondly, do not provide the ideal scenario for a comparison of native and post-AA conditions. The leaflets' reconstruction represents the major obstacle in creating a patient-specific model and their modelling still presents some challenges, specifically in the closing phase. The adoption of multi-modality imaging to complement the geometrical information and improve the computational simulation would be relevant for future studies. Indeed, the current FSI results are notably different from *in vitro* measurements in terms of flow rate, and this could be due to the delayed and slowed valve opening dynamics in the FSI model. This also confirms that the use of digital twins, such as the one presented in this case, presents valid results only when a proper validation and uncertainty quantification is performed. However, due to its ability to provide complementary information to clinical and experimental studies, validated digital twins are a powerful tool for ongoing clinical trials on external AA. Lastly, in this study, only MRI 2D flow could be used to evaluate the outcomes of FSI simulations outcomes, as it was not feasible to calculate the left ventricle outflow tract flow rate from 4D flow MRI, which was limited to qualitative visualization purposes only. A punctual validation of the FSI model is still lacking and represents a further milestone for the reliability of this digital twin. Future studies should aim to validate these findings in human subjects, affected by aortic valve regurgitation, to ensure their applicability to clinical practice.

# 5. Conclusions

This study provides valuable insights into the hemodynamic performance of external single ring AA and establishes a robust framework for future investigations of AA techniques. The development of a porcine-specific AA digital twin represents a significant advancement in cardiovascular research, offering a promising pathway towards the standardization and optimization of AA procedures. Continued research integrating *in vivo*, *in vitro*, and *in silico* methodologies will be essential for further validating these findings and translating them into clinical practice. This framework has been proven suitable for anticipating personalized clinical testing, given the only requisite of patient-specific geometrical information, retrievable from data routinely collected prior to surgery.

# Funding

This research did not receive any specific grant from funding agencies in the public, commercial, or not-for-profit sectors. M. Colombo and P. Johansen acknowledge the support from Aarhus University. G. Luraghi is supported by the European Research Council (ERC, project PROTEGO, G.A. 101162753).

# Conflict of interest

The authors declare that the research was conducted in the absence of any commercial or financial relationships that could be construed as a potential conflict of interest. The authors L. L. Benhassen and P. Johansen have filed a patent application on the new annuloplasty ring design with the intention of pursuing commercialization.

# Author contributions

**MZ**: Conceptualization, Methodology, Formal analysis, Investigation, Data curation, Writing Original Draft, Writing – Review and Editing, Visualization. **LB**: Formal analysis, Investigation, Data curation, Writing – Review and Editing. **SR**: Conceptualization, Investigation, Data curation, Writing – Review and Editing. **GL**: Supervision, Writing – Review and Editing. **LLB**:

Conceptualization, Writing – Review and Editing, Funding acquisition. **PJ**: Conceptualization, Supervision, Methodology, Project administration, Writing – Review and Editing, Funding acquisition. **MC**: Conceptualization, Methodology, Formal analysis, Investigation, Data curation, Writing – Original Draft, Review and Editing, Supervision, Project administration, Funding acquisition.

All authors contributed to the article and approved the submitted version.

# References


1 J. S. Aluru, A. Barsouk, K. Saginala, P. Rawla and A. Barsouk, *Medical Sciences (Basel, Switzerland)*, 2022, 10, 32, 10.3390/medsci10020032.

2 J. Vojacek, P. Zacek and J. Dominik, Eds., Aortic Regurgitation, Springer, Cham, 1st ed. 2018 edition., 2018, 978-3-319-74212-0.

3 E. Lansac, I. Di Centa, F. Raoux, N. Al Attar, C. Acar, T. Joudinaud and R. Raffoul, *European Journal of Cardio-Thoracic Surgery*, 2008, 33, 872–878; discussion 878-880, 10.1016/j.ejcts.2007.12.033.

4 J. S. Rankin, D. Mazzitelli, M. Gerdisch, R. S. Downey, G. B. Blossom, G. Stavridis, T. J. M. Fischlein, L. M. Wei, J. I. Sáez de Ibarra Sanchez and V. Badhwar, *Cirugía Cardiovascular*, 2023, 30, S60–S68, 10.1016/j.circv.2023.05.003.

5 E. Lansac, *European Journal of Cardio-Thoracic Surgery*, 2006, 29, 537–544, 10.1016/j.ejcts.2005.12.055.

6 M. A. Noor, L. L. Benhassen, A. E. Kaspersen, M. G. Weiss, J. M. Hasenkam and P. Johansen, *Journal of Cardiovascular Translational Research*, 2023, 16, 1144–1152, 10.1007/s12265-023-10393-7.

7 L. de Kerchove, R. Vismara, A. Mangini, G. B. Fiore, J. Price, P. Noirhomme, C. Antona and G. El Khoury, *European Journal of Cardio-Thoracic Surgery*, 2012, 41, 1117–1124, 10.1093/ejcts/ezr237.

8 L. L. Benhassen, J. H. Hedensted, M. Sharghbin, T. Bechsgaard, S. L. Nielsen, J. M. Hasenkam and P. Johansen, *European Journal of Cardio-Thoracic Surgery*, 2023, 63, ezad164, 10.1093/ejcts/ezad164.

9 U.S. Congress. FDA Modernization Act 2.0. Public Law 117-328. 136 Stat. 4459. Enacted December 29, 2022.

10 A. D. Kaiser, N. K. Schiavone, C. J. Elkins, D. B. McElhinney, J. K. Eaton and A. L. Marsden, *Annals of Biomedical Engineering*, 2023, 51, 2267–2288, 10.1007/s10439-023-03266-2.

11 L. Bontempi, M. Zattoni, A. Ramella, F. Migliavacca, S. Ringgaard, W. Y. Kim, P. Johansen and M. Colombo, *Computers in Biology and Medicine*, 2025, 192, part B, 10.1016/j.compbiomed.2025.110398.

12 L. L. Benhassen, J. H. Hedensted, M. Sharghbin, S. N. Skov, L. Carlson Hanse, M. J. Tjørnild, T. Bechsgaard, D. M. Ropcke, S. L. Nielsen and J. M. Hasenkam, *European Journal of Cardio- Thoracic Surgery*, 2020, 57, 1210–1217, 10.1093/ejcts/ezaa001.

13 S. Morganti, M. Conti, M. Aiello, A. Valentini, A. Mazzola, A. Reali and F. Auricchio, *Journal of Biomechanics*, 2014, 47, 2547–2555, 10.1016/j.jbiomech.2014.06.007.

14 R. M. Lang, B. P. Cholley, C. Korcarz, R. H. Marcus and S. G. Shroff, *Circulation*, 1994, 90, 1875–1882, 10.1161/01.CIR.90.4.1875.

15 Z. R. Liu, C. T. Ting, S. X. Zhu and F. C. Yin, *Hypertension*, 1989, 14, 129–136, 10.1161/01.HYP.14.2.129.

16 ISO 37-1:2017, 'Rubber, vulcanized or thermoplastic - determination of tensile stress-strain properties'.

17 ISO 5910:2018, 'Cardiovascular implants and extracorporeal systems - Cardiac valve repair devices'.

18 G. Luraghi, F. Migliavacca and J. F. Rodriguez Matas, *Cardiovascular Engineering and Technology*, 2018, 9, 723–738, 10.1007/s13239-018-00373-3.

19 R. Jonnagiri, E. Sundström, E. Gutmark, S. Anderson, A. S. Pednekar, M. D. Taylor, J. T. Tretter and I. Gutmark-Little, *Medical & Biological Engineering & Computing*, 2023, 61, 1489–1506, 10.1007/s11517-023-02790-6.

20 A. F. Stalder, M. F. Russe, A. Frydrychowicz, J. Bock, J. Hennig, and M. Markl, *Magnetic Resonance in Medicine*, 2008, 60, 1218-1231, 10.1002/mrm.21778.

21 J. Garcia, A. J. Barker, J. D. Collins, J. C. Carr and M. Markl, *Magnetic resonance in medicine*, 2017, 78, 689–701, 10.1002/mrm.26387.

22 M. Colombo, M. Bologna, M. Garbey, S. Berceli, Y. He, J. F. Rodriguez Matas, F. Migliavacca and C. Chiastra, *Medical Engineering & Physics*, 2020, 75, 23–35, 10.1016/j.medengphy.2019.10.005.

23 F. Sturla, E. Votta, M. Stevanella, C. A. Conti and A. Redaelli, *Medical Engineering & Physics*, 2013, 35, 1721–1730, 10.1016/j.medengphy.2013.07.015.

24 G. Marom, *Archives of Computational Methods in Engineering*, 2015, 22, 595–620, 10.1007/s11831-014-9133-9.

25 Z. Yin, C. Armour, H. Kandail, D. P. O'Regan, T. Bahrami, S. Mirsadraee, S. Pirola and X. Y. Xu, *International Journal for Numerical Methods in Biomedical Engineering*, 2024, 40, e3865, 10.1002/cnm.3865.

26 I. S. Lan, J. Liu, W. Yang, J. Zimmermann, D. B. Ennis and A. L. Marsden, *Annals of Biomedical Engineering*, 2023, 51, 377–393, 10.1007/s10439-022-03038-4.

27 J. Zimmermann, K. Bäumler, M. Loecher, T. E. Cork, A. L. Marsden, D. B. Ennis and D. Fleischmann, *Scientific Reports*, 2023, 13, 22557, 10.1038/s41598-023-49942-0.

28 L. Christierson, P. Frieberg, T. Lala, J. Töger, P. Liuba, J. Revstedt, H. Isaksson and N. Hakacova, *Computers in Biology and Medicine*, 2024, 171, 108033, 10.1016/j.compbiomed.2024.108033.

The final published version is available at https://doi.org/10.1016/j.cmpb.2026.109246

# Figure captions

**Figure 1:Workflow of the study and software**. Segmentation and post-processing of in vivo MRI data to produce porcine-specific CAD models of the AR used in flow-loop experiments and FSI simulations. Comparison of computational results with in vivo porcine data to assess the fidelity of AA digital twin.

**Figure 2: *In vitro* investigation.** A) Resin phantoms fabrication steps from CAD model design, to support placing, 3D printing and UV curing. B) CAVELab MCL set up consisting of AR phantom (A), fluid-filled pressure sensors (B), compliance chamber (C), peripheral resistance clamp (D), electromechanical piston pump (E), atrial chamber (F), ventricular chamber (G) and flowmeter (H).

**Figure 3: *In silico* model.** A) Different components of the native computational model meshed with triangular shells. B) Pressure boundary conditions imposed at the inlet (ventricular pressure, $p_{in}$) and outlet (aortic pressure, $p_{out}$) of the native model in the FSI simulations.

**Figure 4: Hemodynamic results on cut planes**. A) Scheme of cut planes and clip volumes considered during results post-processing and data visualization. B) Velocity magnitude contour plots for native and post-AA models at peak systole. C) Velocity and vorticity magnitude median results on mid and top cut planes at peak systole and late diastole for native and post-AA models. D) Velocity magnitude distribution on top, mid and bottom planes at peak systole in native and post-AA models. Results are compared with normalized results with respect to the bottom plane area. *: $p$-value < 0.05; **: $p$-value < 0.0005; n.s.: not significant.

**Figure 5: Hemodynamic results on clip volumes**. A) Median LNH results on clip volumes for native and post-AA models at peak systole and late diastole. B) LNH threshold visualization of values above 0.7 at peak systole for native and post-AA models. C) Normalized WSS contour plots at peak systole for native and post-AA models. D) WSS distributions on clip volumes for native and post-AA models normalized with respect to the maximum WSS value for each case.

**Figure 6: Structural results on aortic leaflets**. A) Visualization of aortic leaflets opened and closed configuration during experiments for native and post-AA models. B) Visualization of aortic leaflets Von Mises stress for native and post-AA AR models at peak systole and end diastole. C) Midpoint radial displacement results throughout the third cardiac cycle for right coronary (RCL), left coronary (LCL) and non-coronary (NCL) leaflets in native model. D) Midpoint radial displacement results throughout the third cardiac cycle for right coronary (RCL), left coronary (LCL) and non-coronary (NCL) leaflets in post-AA model.

**Figure 7: MRI-based assessment of hemodynamic results**. A) MRI view of the porcine hearts showing the positioning of the two available planes to compute AR flow rate waveform with respect to the segmented models from in vivo MRI data (green: Qoutflow; light blue: Qinflow). B) Out-of-plane velocity component contour plots for FSI simulations and MRI in vivo data at the outlet of the AR for native and post-AA models. Contour plots are reported with the same orientation, which is detailed in the two maps on the left of the figure for both MRI and FSI (A: anterior; P: posterior; R: right; L: left).